

<https://doi.org/10.1038/s42003-025-08338-8>

Super-enhancers orchestrate transcriptional dysregulation and metabolic reprogramming in uveal melanoma



Hui Pan^{1,2,4}, Weihuan Shao^{1,2,4}, Huixue Wang^{2,3,4}, Shengfang Ge^{1,2}, Lingyu Zhang^{1,2}, Xiaofang Xu^{1,2}✉, Yefei Wang^{1,2}✉ & Ai Zhuang^{1,2}✉

Uveal melanoma (UM) is the most common intraocular malignancy in adults and frequently metastasizes. Somatic mutations and chromatin aberrations have been implicated in the pathogenesis of this deadly disease. Despite rapid progress in elucidating the genetic landscape of UM, the epigenetic architecture underlying UM pathogenesis remains incompletely understood. Here, we describe a super-enhancer-mediated epigenetic pipeline through genome-scale histone acetylation and transcriptional profiling. We first characterized the active landscape of super-enhancer profiles in UM via chromatin immunoprecipitation sequencing (ChIP-seq). We identified master transcription factors specifically driven by UM-specific super-enhancers, and our pipeline identified transcription factor AP-2 alpha (TFAP2A), which is highly associated with metabolism and oncogenesis, as the top essential regulator in UM. TFAP2A occupied predicted super-enhancers associated with the oncogene *Solute Carrier Family 7 member 8* (SLC7A8) in UM, thereby elucidating a mechanism for regulating oncogene expression. Collectively, our data illustrate the potential for epigenetic targeting of super-enhancer-mediated oncogene dependencies in UM, highlighting an epigenetic vulnerability that can be exploited for precision therapy.

Uveal melanoma (UM) is the most common intraocular malignancy in adults. The incidence of UM ranges from 1–9 per million people annually worldwide, with approximately 6 per million people in Europe and the USA, and 0.5 per million people in Asia and Africa¹. UM exhibits a considerable propensity for metastasis, and once metastasis spread is detected, the median survival time is less than one year². Unlike cutaneous melanoma, which harbours mutations in proto-oncogenes such as *BRAF*, *NRAS* and *KIT*, UM harbours exclusive oncogenic mutations in *G protein subunit alpha q* (*GNAQ*), *G protein subunit alpha 11* (*GNAI1*)³, *phospholipase C beta 4* (*PLCB4*) or *cysteinyl leukotriene receptor 2* (*CYSLTR2*)^{4,5}. Furthermore, genetic variants such as monosomy 3 and *BRCA1-associated protein 1* (*BAP1*) mutations and gene expression profiles (GEPs) are well recognized for their role in UM progression^{6–8}.

Recently, some progress has been made in the study of epigenetic mechanisms in UM^{9,10}. A unique DNA methylation profile in UM has been demonstrated¹¹. Furthermore, a comprehensive epigenetic study revealed that UM progression is largely driven by the loss of activity of Polycomb Repressive Complex 1 (PRC1), a key transcriptional regulator in development that modulates chromatin structure and catalyses histone H2A lysine 119 ubiquitination (H2AK119ub1)¹². Preclinical experiments have revealed that small-molecule epigenetic drugs targeting epigenetic factors involved in histone modification, such as histone deacetylases (HDACs) and the bromodomain and extraterminal domain (BET) family, display robust efficiency in the therapeutic intervention of UM^{13,14}. Epigenetic dysregulation is involved in the development of UM, which affects chromatin structure and gene transcriptional activity, thereby activating oncogenes or repressing tumour suppressor genes, thus promoting UM cell proliferation, migration and

¹State Key Laboratory of Eye Health, Department of Ophthalmology, Ninth People's Hospital, Shanghai Jiao Tong University School of Medicine, Shanghai, China.

²Shanghai Key Laboratory of Orbital Diseases and Ocular Oncology, Shanghai, China. ³Department of Ophthalmology, Tongren Hospital, Shanghai Jiao Tong University School of Medicine, Shanghai, China. ⁴These authors contributed equally: Hui Pan, Weihuan Shao, Huixue Wang. ✉e-mail: xuxu0139@hotmail.com;

pap34@163.com; aizh9h@163.com

invasion by activating downstream signalling pathways¹⁰. Despite considerable advances in elucidating the carcinogenesis of UM, the comprehensive epigenetic landscape has not yet been fully characterized. Emerging evidence suggests that epigenetic dysregulation not only contributes to tumorigenesis but may also be implicated in the molecular mechanisms underlying metastatic progression^{15,16}.

Super-enhancers (SEs) are key epigenetic regulators that drive oncogene expression during the initiation and progression of malignancies^{16–19}. Aberrant SEs are markedly enriched with histone modifications to drive the expression of oncogenes²⁰. The transcription of SE-related oncogenes depends on the recruitment of master transcription factors (MTFs) and cofactors. Notably, MTFs regulate core oncogenes, for example, the MTF Kruppel-Like Factor 3 (KLF3) has been implicated in colorectal cancer²¹. In particular, oncogenes driven by SEs are vulnerable to MTF suppression^{19,22}. Such epigenetic vulnerabilities have been demonstrated in several malignancies¹⁸. For instance, the fusion protein PAX3-FOXO1 establishes a myoblastic SE landscape and shows a profound dependence on BET family inhibitors in specific rhabdomyosarcoma patients²³.

Here, we applied an integrative analytic pipeline of epigenetic and transcriptomic profiles to define UM-specific SEs and potential therapeutic targets. MTFs that are differentially expressed in UM were found to preferentially enrich oncogene-associated SEs. Subsequent bioinformatic analysis revealed the critical node-transcription factor AP-2 alpha (TFAP2A) as the main lineage-specific factor in UM, and its high-confidence targets were identified. TFAP2A is a key MTF that is highly expressed in UM and is closely associated with UM oncogenesis. Using CRISPR/Cas9 genomic editing, we eliminated TFAP2A expression and observed a significant reduction in tumour formation and cellular nutrient metabolism, suggesting its oncogenic properties. Pathway analysis and functional studies also revealed TFAP2A as the crucial node driving metabolic reprogramming. Moreover, we revealed Solute Carrier Family 7 member 8 (SLC7A8) as a key TFAP2A-occupied SE that contributes to UM tumorigenesis. Taken together, the results of our study revealed a UM-specific SE regulatory circuit that regulates UM oncogenesis and metabolic reprogramming.

Methods

Cell culture

The normal human melanocyte cell line PIG1 was provided by the Department of Ophthalmology, Peking University Third Hospital (Beijing, China). The UM cell lines 92.1 and MP46 and the human retinal pigment epithelial cell lines ARPE19 and HEK293T were purchased from American Type Culture Collection (Manassas, VA, USA). The human UM cell lines OMM2.3, OMM1 and Mel290 were provided by Professor Martine J Jager (Leiden University Medical Center, Leiden, The Netherlands).

PIG1 cells were cultured in DMEM/Ham's F12K medium (GIBCO, Thermo Fisher Scientific, Waltham, MA, USA). HEK293T and Mel290 cells were cultured in DMEM (GIBCO), and the human UM cell lines 92.1, MP46, OMM1 and OMM2.3 were cultured in RPMI-1640 medium (GIBCO). All media were supplemented with 10% foetal bovine serum (GIBCO), penicillin (100 U/mL) and streptomycin (100 mg/mL). The cells were cultured at 37 °C in a humidified 5% CO₂ atmosphere. All the in vitro cell lines were validated by short tandem repeat profiling and confirmed to be mycoplasma free.

Tissue specimens

Tumour samples were collected from surgically resected tumours by enucleation or endoresection at the Department of Ophthalmology, Ninth People's Hospital, Shanghai Jiao Tong University School of Medicine (Shanghai, China). Fresh samples were snap-frozen and stored in liquid nitrogen. Written informed consent for this study was obtained from all patients in Shanghai Ninth People's Hospital, Shanghai Jiao Tong University School of Medicine. All ethical regulations relevant to human research participants were followed. The study was in accordance with the Declaration of Helsinki and approved by the Ethics Committee of Shanghai

Ninth People's Hospital, Shanghai Jiao Tong University School of Medicine (approval No. SH9H-2019-T185-2).

Lentivirus production and CRISPR-Cas9 transfection

HEK293T cells were cotransfected with the lentiviral envelope and packaging plasmid pCMV-VSVG (Addgene plasmid #8454), psPAX2 (Addgene plasmid #12260) or the lenti-CRISPR plasmid of sgRNA (Supplementary Table S1) and Lipofectamine 3000 (Invitrogen, Carlsbad, CA, USA). Twenty-four hours after transfection, the medium was replaced, and three days after transfection, the medium was centrifuged. The supernatant was collected, filtered and concentrated using Amicon Ultra tubes (100 kDa, Merck-Millipore, Darmstadt, Germany). The cells were seeded in 24-well plates and transduced with lentivirus containing 8 g/ml polybrene. Stable clones were selected using puromycin.

Western blotting

For western blotting, UM cells were harvested and washed twice with ice-cold PBS. The cells were lysed in RIPA lysis buffer supplemented with proteinase inhibitor cocktail and phosphatase inhibitor cocktail (Roche, Basel, Kanton Basel, Switzerland). Protein concentrations were determined with a Bio-Rad protein assay kit (Bio-Rad Laboratories, Hercules, CA) according to the following protocol. The samples were denatured at 95 °C for 10 min and separated by sodium dodecyl sulfate–polyacrylamide gel electrophoresis, followed by transfer to a nitrocellulose membrane (Bio-Rad). The membrane was incubated with primary antibody overnight at 4 °C. The membrane was then incubated with secondary antibody for 1 h at room temperature. Antibodies against the following antigens were used: TFAP2A (1:1000, 10319-3-ap, Proteintech), Actin (1:1000, ab8226, Abcam), Anti-rabbit IgG (H + L) (Alexa Fluor® 488 Conjugate) (1:5000, 4412S, Cell Signaling Technology).

RNA-seq

RNA was extracted using the RNeasy Mini Kit (Qiagen, Hilden, Germany), and 1 ng of RNA was used to construct the sequencing library using the KAPA Stranded RNA-seq Library Prep Kit (Illumina, San Diego, CA, USA). The generated library was evaluated using an Agilent 2100 Bioanalyzer and quantified via a qPCR technique. The barcoded libraries were combined, captured on an Illumina flow cell and then sequenced for 150 cycles from both ends on an Illumina Novaseq 6000 instrument. FastQC was used to perform quality control and cutadapt was used to remove the adaptors²⁴. The trimmed paired-end reads were then aligned to the GRCh37 reference genome using HISAT2 v2.1.0. Each transcript abundance was assessed using StringTie, and the fragments per kilobase of exon model per million mapped fragments (FPKM) value for each gene and transcript was determined using the Ballgown package in R. Gene Ontology and pathway analyses were conducted, and volcano plots were generated using R. Differential gene expression analysis was performed using DESeq2 v3.7. Heatmaps were generated using the R package pheatmap. Curated gene sets (Molecular Signatures Database v6.2) were analysed using GSEA software version 3.0. The GSEA preranked instrument was applied with 1000 permutations, and only gene sets with a maximum list size of 500 and a minimum list size of 15 were taken into account. A pan-cancer analysis was conducted using the UCSCXenaShiny to explore gene expression patterns across multiple cancer types²⁵. Additionally, TFAP2A genomic alterations, including copy number variations (CNVs), were analyzed using the cBioPortal platform²⁵.

RNA extraction and real-time PCR(RT–PCR)

RNA was extracted using TRIzol and measured using a NanoDrop ND-2000 (NanoDrop, Waltham, MA, USA). One microgram of RNA was treated with DNase (Invitrogen, Carlsbad, CA, USA). For reverse transcription, cDNA generation was performed using PrimeScript RT Master Mix (Takara, Kyoto, Japan). SYBR Green PCR Master Mix (Takara) was used for RT-PCR analysis. The target genes were amplified on a 7500 Fast Real-Time PCR machine (Applied Biosystems, Foster City, CA, USA). The

experiments were repeated in triplicate. The primers used are listed in Supplementary Table 3.

Chromatin immunoprecipitation sequencing (ChIP-seq)

ChIP-seq experiments were carried out with the ChIP-IT High Sensitivity Kit (Active Motif #53040) following the manufacturer's protocol. Briefly, UM cells were cultured to 90% confluence, treated with 1% formaldehyde for 10 min and quenched with 125 mM glycine. Cells were washed twice with cold PBS, harvested, and lysed in Lysis Buffer supplemented with protease inhibitors. Chromatin was sheared using an EpiShear Probe Sonicator with 4 cycles of 30 s ON/30 s OFF pulses at 30% amplitude until DNA fragments reached 200–500 bp. After centrifugation, 50 µg of chromatin was immunoprecipitated overnight at 4 °C with 5 µg of target-specific antibody in ChIP Buffer. Immune complexes were captured with Protein G Magnetic Beads for 1 h at 4 °C, followed by sequential washes with Low Salt Wash Buffer and High Salt Wash Buffer. DNA was eluted in Elution Buffer and reverse crosslinked at 65 °C overnight. For library preparation, purified ChIP DNA fragments were size-selected (250–300 bp) using SPRIselect beads. Libraries were quantified by Qubit fluorometry (Thermo Fisher) and quality-checked by Agilent Bioanalyzer. Multiplexed libraries were sequenced on an Illumina NovaSeq 6000 system using the S4 flow cell, generating paired-end reads (2 × 150 bp) per sample. Antibodies against the following antigens were used: Histone H3 (tri methyl K9) (5 µg, ab176916, Abcam), Histone H3 (mono methyl K4) (5 µg, ab176877, Abcam), Histone H3 (tri methyl K27) (5 µg, ab192985, Abcam), Histone H3K27ac (5 µg, 39034, Active Motif), p300 (5 µg, 61401, Active Motif).

ChIP-seq analysis

The reads were mapped to the reference genome using BWA (v 0.7.17). MACS2 (<https://github.com/taoliu/MACS/>) was used to call peaks, with input used as a control. Gene ontology was analysed using the online tool GREAT, with the whole genome used as the background. Chromatin states were investigated using ChromHMM (<http://compbio.mit.edu/ChromHMM/>). Bedtools (<http://bedtools.readthedocs.io/en/latest/>) was used to find differential peaks and to determine normalized per million mapped reads (RPM), and enhancers were mapped to their nearest gene using the EDEN protocol according to previous methods²³. Known and de novo motif enrichments were identified using HOMER and MEME. Enrichment peaks were visualized with IGV tools. For enhancer calling and enhancer-gene associations, the Rank Ordering of Super-Enhancers (ROSE) algorithm was used to call enhancers and SEs according to H3K27ac enrichment in UM cells. ChIP-seq occupancy heatmaps and meta-profile plots were prepared using deepTools. Consensus TF DNA binding motifs (De Novo) were investigated using a 1 kb window centred on significant peaks using the HOMER suite. Gene ontology classification was performed using the Gene Ontology (GO) molecular function ontologies. P values were adjusted using the Benjamini–Hochberg multiple testing correction.

Cleavage under targets and tagmentation (CUT&Tag)

The CUT&Tag assay was completed as previously described²⁶. Generally, 50 mg of tissue was collected, washed and mixed with activated concanavalin A-coated magnetic beads (Bangs Laboratories, Inc., Fishers, IN, USA.) at room temperature for 15 min. The mixture was resuspended in 100 µl DIG-wash buffer containing 2 mM EDTA and primary antibody (1:50 dilution) and incubated overnight at 4 °C. The secondary antibody was added at 1:50 dilution and incubated at room temperature for 1 h. After washing, 100 µl pA-Tn5 adapter complex (~40 nM) was added and incubated at room temperature for about 1 h. After washing, the cells were resuspended in Tagmentation buffer (50 µl) and incubated at 37 °C for 1 h. Then, Proteinase K treatment was used at 55 °C for 30 min to terminate the tagmentation, followed by 70 °C incubation for 20 min to inactivate Proteinase K. DNA was then extracted with AMPure XP beads (Beckman Coulter) and eluted. Sequencing was conducted on the Illumina NovaSeq 6000 system with 150-bp paired-end reads. Differentially accessible peaks

were identified using thresholds of fold change >2.0 (log₂ ratio > 1) and *p*-value < 0.05. Antibodies against the following antigens were used: Histone H3K27ac (1:50, 39034, Active Motif), Anti-rabbit IgG (1:50, 4412S, Cell Signaling Technology).

Assay for transposase-accessible chromatin with high-throughput sequencing (ATAC-seq)

ATAC-seq was conducted according to the manufacturer's instructions. Briefly, UM cells were trypsinized and collected. The Tn5 transposition reaction was performed using the Nextera kit (Illumina). DNA was purified using the MinElute Kit (Qiagen). Library amplification was performed using NEBNext High-Fidelity 2X PCR Master Mix (NEB) with SYBR Green I dye (Invitrogen) and Nextera primers at 25 µM. Amplified libraries were purified with a PCR purification kit (Qiagen), and quality control was performed using the 2200 TapeStation (Agilent). Libraries were sequenced using Illumina NextSeq 500 paired-end 150-bp reads.

In vivo studies

Nude mouse models (6–8 weeks, female) were established by injecting 1 × 10⁶ sgNC or sgRNA cell lines (OMM2.3-sgTFAP2A-1/2) into the tail vein. The fluorescence intensity of the tumours was measured every 7 days for a total of 30 days. At the end of the experiments, the mice were sacrificed, and the tumours were collected for further analysis. We have complied with all relevant ethical regulations for animal use. All experimental procedures were approved by the Institutional Animal Care and Use Committee of the Ninth People's Hospital, Shanghai JiaoTong University School of Medicine. According to the institutional guidelines, the maximal permitted tumor diameter for subcutaneous xenografts was 20 mm (or approximately 4000 mg in mass). In all experiments, tumor growth remained within these approved limits.

Gas chromatography–mass spectrometry (GC–MS)

A total of 1 × 10⁶ cells were harvested and washed three times with PBS, and metabolites were collected by adding 1 ml of ice-cold extraction buffer (50% methanol, 30% acetonitrile, and 20% water). The supernatant was obtained by centrifugation at 12,000 rpm for 10 min at 4 °C, and transferred to GC-compatible vials. The samples were stored at –80 °C. Prior to GC–MS analysis, MS data were obtained. A Thermo Scientific Trace 1310 Gas Chromatograph coupled with a Thermo Scientific ISQ™ QT Mass Spectrometer was used for the analysis. The data were analysed using Thermo TraceFinder version 4.0 software.

Luciferase reporter assays

Luciferase assays were performed in UM cells with the reporter 8xGTIIc-Lux. The luciferase reporter was transfected together to normalize for transfection efficiency. Firefly luciferase activity was measured with an Infinite F200PRO plate reader using luciferin as a substrate. The data are presented as firefly/β-galactosidase activity. Each sample was transfected in triplicate, and this process was repeated three times.

Metabolite change measurement

The cells were seeded in 6-well plates and allowed to adhere overnight. The following day, the culture medium was replaced with fresh medium, and the cells were incubated for an additional 24 h. Glucose uptake was determined using the Glucose Uptake Colorimetric Assay Kit from BioVision (catalogue number K676-100). The absorbance was measured at 450 nm using a microplate reader. Lactate secretion was measured using the Lactate Colorimetric Assay Kit from BioVision (catalogue number K627-100). The absorbance was measured at 450 nm. Glutamine uptake was determined using the Glutamine/Glutamate Determination Kit from Sigma-Aldrich (catalogue number GLN1). The absorbance was measured at 340 nm.

Colony formation

Cell colony formation was detected via crystal violet staining. A volume of 1 mL of complete medium containing 1 × 10³ cells was added to each well of

a 6-well plate. The plate was stained with 0.25% crystal violet after 1–2 weeks.

Flow cytometry assay

OMM1, OMM2.3 and PIG1 cells (3×10^4) were cultured in 24-well plates overnight. Following digestion with 0.25% trypsin (without EDTA) and washing with PBS, apoptosis was identified by double staining with Annexin V-FITC and propidium iodide (BD Biosciences, USA). Apoptosis and cell cycle were quantified using a flow cytometer (FACSCalibur, BD Biosciences, USA) and analyzed using the FlowJo software.

Statistics and reproducibility

GraphPad Prism 7 (GraphPad Software) was used for statistical analysis. All of the experiments were performed in triplicate, and the data are presented as the means \pm standard deviations (SDs). The comparative threshold cycle method was used according to the $\Delta\Delta$ threshold cycle method. The differences between two groups were analysed with the unpaired two-sided Student's t-test or the Mann-Whitney U test. A p -value < 0.05 was considered statistically significant and is indicated with asterisks. All experiments utilized 2–10 replicates and are representative of multiple independent experiments (typically 3).

Reporting summary

Further information on research design is available in the Nature Portfolio Reporting Summary linked to this article.

Results

Active landscape of SE profiles in uveal melanoma

H3K27ac is a key characteristic of enhancers, particularly SEs, which are defined as having strong enrichment over extended regions²⁷. To explore active enhancer profiles in UM, we designed an epigenomic pipeline to identify SE regulators in UM (Fig. 1A). First, using normal melanocytes as a comparator, we defined enhancers with recurrently gained activity across UM cell lines (Fig. 1B) by ChIP-seq. A total of SE-associated genes were found in OMM1, 92.1 and OMM2.3 cells, with 1,085 identified in OMM1, 1422 in 92.1, and 1303 in OMM2.3, respectively. Intriguingly, most SEs occupied some known lineage genes involved in melanocyte differentiation and melanin production, such as *tyrosinase-related protein 1* (*TYRP1*), *melanocyte-inducing transcription factor* (*MITF*) and *melan-A* (*MLANA*) (Fig. 1B). We also revealed that oncogenes such as *TFAP2A*, *RAS* *guanyl releasing protein 3* (*RASGRP3*), *sex determining region Y-box transcription factor 10* (*SOX10*) and *MITF* (Fig. 1C) were significantly enriched in UM cells. In contrast, H3K27ac signals were low in the corresponding genes in normal melanocytes (Fig. 1B). *TFAP2A* is a transcription factor (TF) that binds to specific regions of DNA to control gene expression, notably to regulate melanocyte differentiation²⁸. Our data suggest that SE regulatory elements represent active chromatin marks on lineage-specific genes and oncogenes.

TFs tend to bind to enhancers and SEs to define the cell fate, among which MTFs are produced at extremely high levels and can bind most of the enhancers in a stoichiometric manner. In accordance with the established MTF identification pipeline²³ for tumours (Fig. 1D), we identified the MTFs regulated by SEs that presented considerable pattern enrichment in enhancers. These MTFs also presented relatively high levels of expression (average FPKM > 20) and were more highly expressed than in normal tissues. The results revealed a list of 26 TFs that were consistently over-expressed, suggesting a convergent underlying epigenetic state. Since MTFs are expressed at high concentrations to maintain their enrichment, we then filtered TFs with low expression levels as well as those expressed in normal cells (cutoff FPKM > 20). Therefore, we generated a series of potential TFs with significantly high levels of lineage-specific expression compared with those in normal tissues. Compared with normal choroidal tissue, MTFs presented significant motif enrichment in enhancers. In particular, motif analysis revealed significant enrichment of *MITF* and *TFAP2A* binding sequences in UM cell lines (medium-log p value: tumour 193.3; normal

56.49) (Fig. 1E), indicating that the recognition sequences of *TFAP2A* were highly significantly enriched at SE locations according to motif analysis. Taken together, these results revealed that *TFAP2A*, as a core MTF, was strongly enriched in SEs.

Biological features of SE-associated transcripts

Using an integrative analysis of epigenetic and transcriptional profiles, we identified an SE-driven MTF modulator in UM. We first searched for pathways activated by *TFAP2A* via GSEA (Fig. S1A) and predicted *TFAP2A* interactors using the STRING database (Fig. S1B) (<https://string-db.org/network/>), initially exploring the function of the transcription factor *TFAP2A*. Since the most uniquely and highly expressed MTFs were driven by SEs, to further characterize the effects of MTFs on chromatin, we next sought to investigate the histone modifiers H3K27ac and H3K4me1 and the binding of *TFAP2A* and EP300 binding to SEs. To further investigate whether *TFAP2A* expression was driven by an open chromatin structure, we also performed ATAC-seq to identify accessible chromatin regions in UM cells. We integrated these sequencing results in UM cell lines to identify a larger set of targets and enriched sites (Fig. 2A). Our results revealed that *TFAP2A* directly occupies an SE upstream of the *TFAP2A* locus to drive its expression, confirming that this MTF is self-promoted by an SE. The results revealed that accessible regions were cooccupied with H3K27ac and H3K4me1 signals. We next determined whether *TFAP2A* was enriched in promoter and intergenic regions (Fig. 2B). After peak calling, 19,887 ($p < 0.000001$) peaks were found in *TFAP2A* binding regions; these exhibited the highest statistical significance and the highest intensity. Genome-wide, the majority of the *TFAP2A* binding regions were located within introns and intergenic regions. Additionally, using ChromHMM analysis to define active chromatin regions, we found that *TFAP2A* predominantly resides in active transcription start sites and active enhancers, which harbour the active enhancer marks H3K27ac and H3K4me1 (Fig. 2C). Such interactions spanning broad one-dimensional sequence distances complicated the identification of target genes. Next, we determined the occupancy of *TFAP2A* in SEs over typical enhancers. Notably, *TFAP2A* bound a negligible proportion of typical enhancers (21.4%) but an abundance of SEs (61.55%) (Fig. S2A). Its predominance for SEs over typical enhancers was striking. We established the genomic loci within which *TFAP2A* enhancers may exist (Fig. S2B), and we investigated the topologically associated domain (TAD) structure around the *TFAP2A* locus on the basis of Hi-C data from Juicebox (Fig. S2C). We found that *TFAP2A* expression was modulated by a large ~ 2.4 Mb regulatory TAD region, where binding of the enhancer marker H3K27ac was correlated with the expression of *TFAP2A*.

Next, we created a map of enhancers in UM cell lines and tumours, which contained all the enhancer sites. We therefore discovered *TFAP2A*-SE loci that were highly enriched in UM cell lines and overlaid *TFAP2A* occupancy. We also compared the enhancer histone marker H3K27ac with that of *TFAP2A* sites and identified 12,932 *TFAP2A*-colocalized enhancers in the OMM2.3 cell line (Fig. 2D). To further determine whether these findings are applicable to human malignancies and highly relevant to UM oncogenesis, we next used CUT&Tag to examine SE occupancy in UM specimens. As expected, *TFAP2A*-associated SEs were highly enriched in tumours, suggesting their protumorigenic function, and H3K27ac enrichment in UM tumour tissues and cell lines was associated with a specific signal intensity (Fig. 2E).

The activation of *TFAP2A* is correlated with oncogenic activity

To elucidate the mechanism of epigenetic reprogramming mediated by *TFAP2A*, we first examined the expression of *TFAP2A* in UM tissues and adjacent normal choroidal tissues. We used immunofluorescence staining to examine *TFAP2A* expression in vivo. In accordance with the epigenetic results, *TFAP2A* expression was significantly upregulated in tumours and showed stronger nuclear expression in tumours than in normal adjacent control tissues (Fig. 3A). We then quantified the higher expression of *TFAP2A* in tumour tissues (Fig. 3B) and examined the expression of

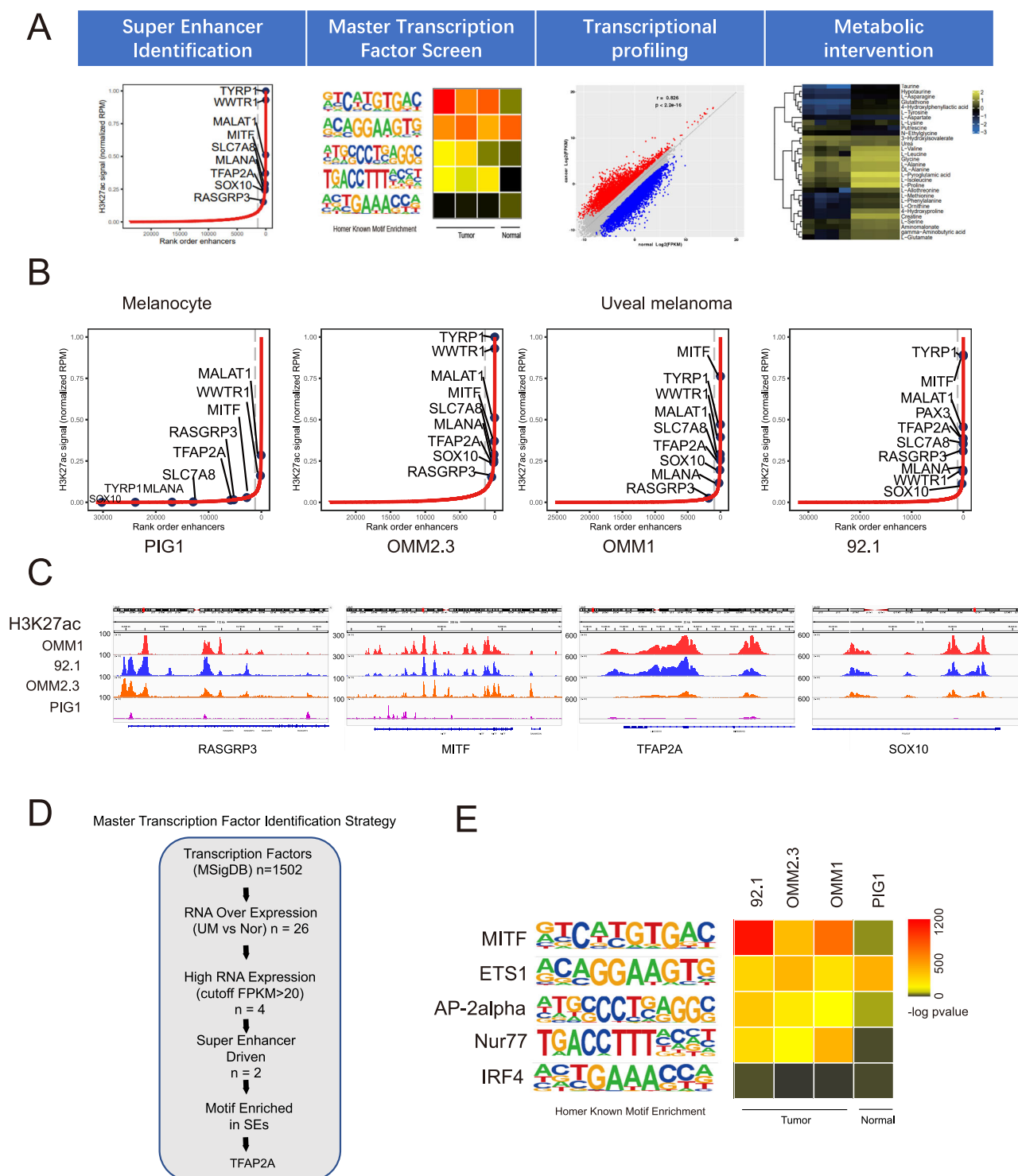


Fig. 1 | The epigenetic landscape of uveal melanoma. A Pipeline of the study. **B** H3K27ac binding at distal enhancers ranked by increasing signal intensity in cell lines. Super enhancers (SEs) were identified as those beyond the inflection point where a rapid increase in signal was observed (indicated by a dashed grey line). TF

genes associated with SEs are indicated in blue. **C** ChIP-seq tracks for the *TFAP2A*, *RASGRP3*, *MITF*, and *SOX10* SE loci. **D** Strategy for discovering master transcription factors (MTFs) from the RNA-seq and ChIP-seq datasets. **E** Motif analysis at the H3K27ac sites in the UM cell lines.

TFAP2A in UM cell lines via RT-PCR analysis (Fig. 3C). The results revealed greater expression of *TFAP2A* in UM cell lines than in normal cell lines. As expected, *TFAP2A* was more highly expressed in most UM specimens, and this conclusion was also verified in the TCGA-UM cohort (Fig. 3D). Since copy number amplification is a common mode of oncogene activation in cancer, we next sought to identify the copy number of the *TFAP2A* gene. SCNA results using pancancer data revealed that the

TFAP2A locus presented a remarkably amplified copy number (Fig. S3B), which was highest in the UM cohort (Fig. S3C). The correlation between *TFAP2A* and gene expression was highly significant (Spearman $r = 0.63$) (Fig. 3E). Multigene analysis also revealed a high frequency of *TFAP2A* amplification in the UM cohort (Fig. 3F). These showed that *TFAP2A* was a crucial master regulator of UM with aberrantly amplified copy numbers and pronounced gene expression.

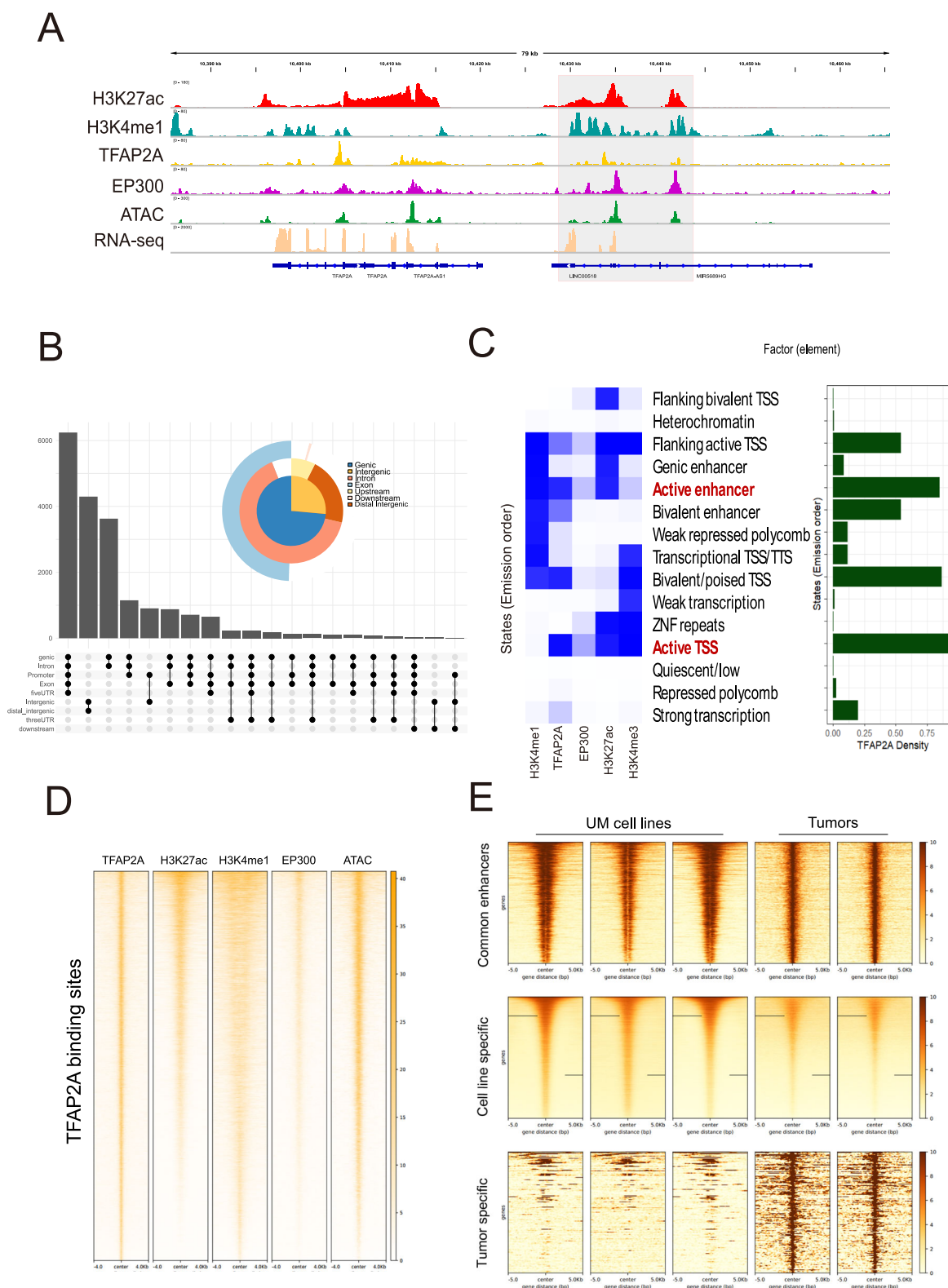


Fig. 2 | TFAP2A-dependent epigenetic transcriptional profiles in UM.

A Normalized ChIP-seq tracks for H3K27ac, H3K4me1, TFAP2A and EP300, ATAC-seq and RNA-seq at the *TFAP2A* loci in OMM2.3 cells; ChIP-seq read signals (y axis) were normalized to the RPKM value in the corresponding sample.

B TFAP2A peak distribution in the OMM2.3 cell line. The scatter plot is accompanied by a bar plot and upset plot showing the amounts of TFAP2A in intronic, exonic, intergenic or promoter-proximal sites. **C** Chromatin states in OMM2.3 cells (left) and relative TFAP2A density (right). States were defined using ChIP-seq data for all histone modifications using the hidden Markov modelling algorithm

(ChromHMM). Frequency refers to the probability of each mark being present in a given state. **D** Heatmaps of TFAP2A density in OMM2.3 cells are shown accordingly. Normalized ChIP-seq tracks for H3K27ac, H3K4me1, and TFAP2A transcription factors at TF2P2A binding loci in OMM2.3 cells. ChIP-seq read signals (y-axis) were normalized to the RPKM value in the corresponding sample.

E Representative heatmaps of H3K27ac density in the OMM2.3 cell line and UM tissue. Differences between cell lines and tumour tissue at common enhancer sites and significantly enriched enhancer sites are shown.

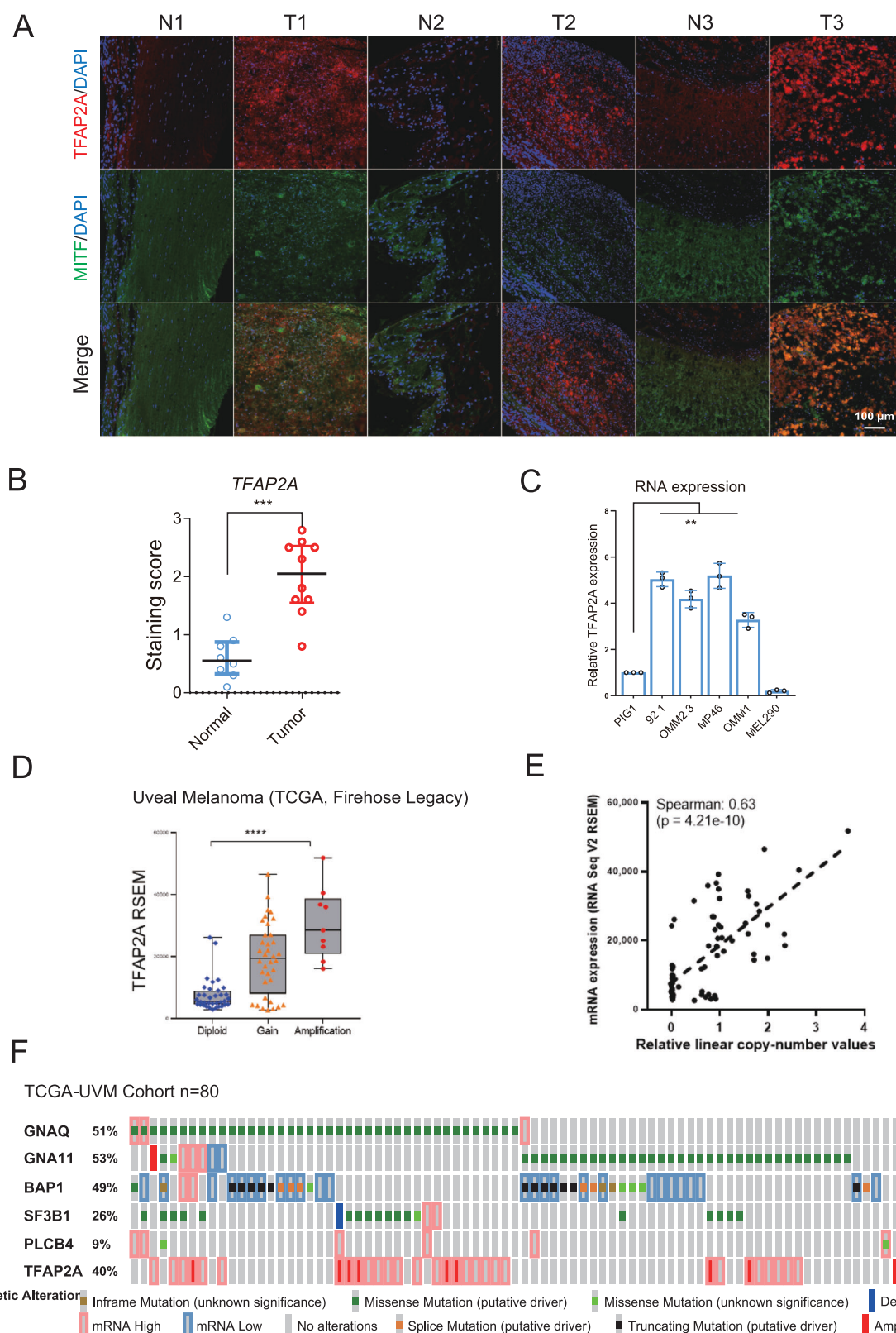


Fig. 3 | Focal amplification drives TFAP2A expression. **A** Representative images of TFAP2A immunofluorescence staining are shown at 20x magnification for UM and normal control samples. **B** TFAP2A immunofluorescence staining of normal and UM tissues. **C** TFAP2A RNA expression was measured in UM cell lines using real-time PCR. * $P < 0.05$, ** $P < 0.01$, *** $P < 0.001$. **D** RNA expression analysis of

TFAP2A expression in the TCGA-UM cohort. The samples were classified according to TFAP2A copy number. **E** Correlations between TFAP2A expression and copy number in the TCGA cohort of UM samples (Spearman correlation, $p < 0.001$). **F** Multigene analysis of UM-specific oncogenes as well as TFAP2A amplification was shown using cBioPortal.

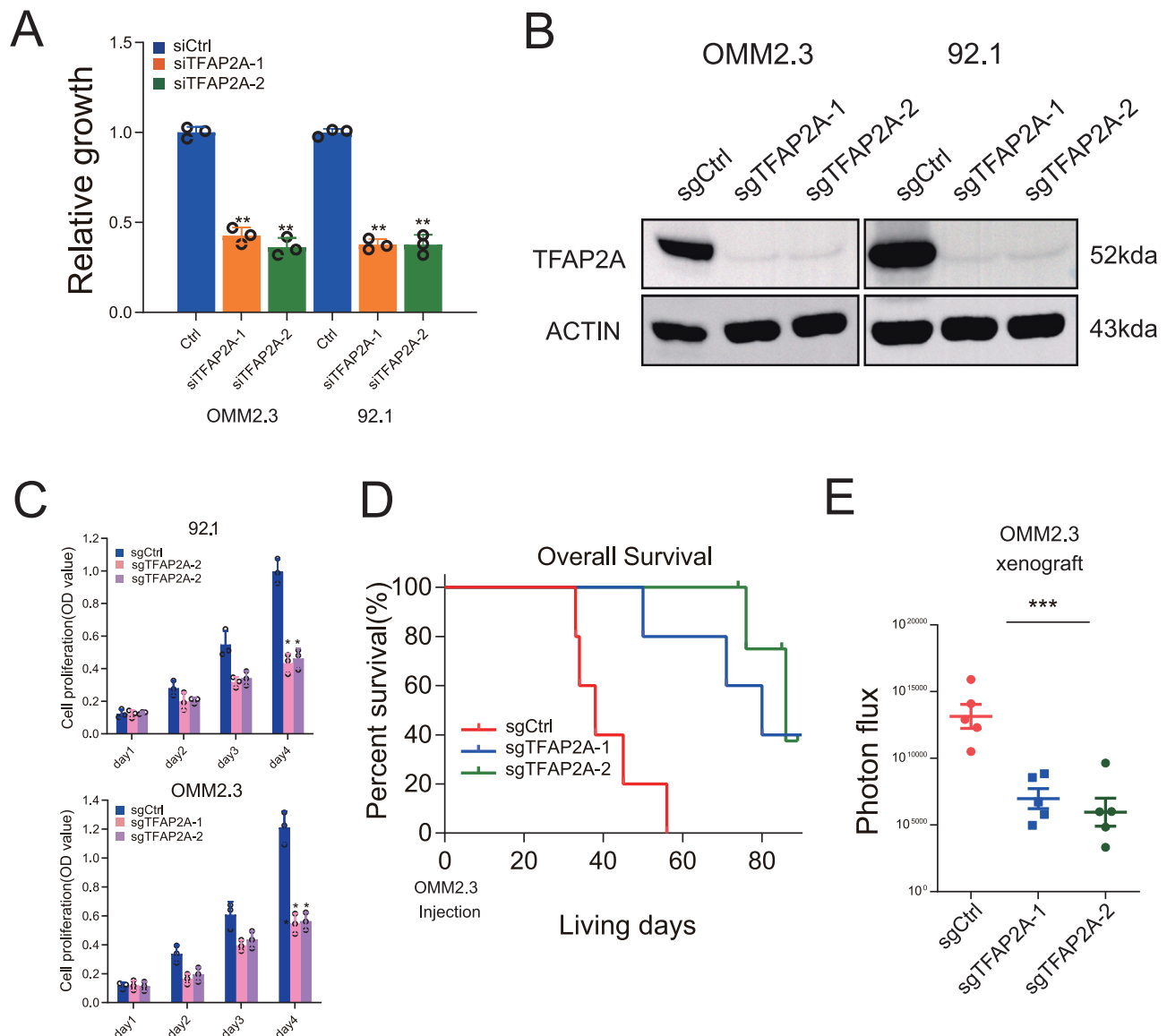


Fig. 4 | *TFAP2A* knockdown suppresses UM tumour growth. **A** CCK8 analysis of OMM2.3 and 92.1 cells transfected with the indicated siRNAs against *TFAP2A*. **B** Western blot analysis of *TFAP2A* expression in cells stably transfected with the indicated sgRNAs. GAPDH was used as a loading control. **C** CCK8 analysis of

OMM2.3 and 92.1 cells stably transfected with the indicated sgRNAs against *TFAP2A*. **D** In vivo tumour formation by OMM2.3 and *TFAP2A*-KD cells. K-M curves for the sgNC and sg*TFAP2A* groups. **E** IVIS signals in the control and *TFAP2A* depletion groups. * $P < 0.05$, ** $P < 0.01$, *** $P < 0.001$.

TFAP2A promotes UM formation in vitro and in vivo

The above findings prompted us to propose *TFAP2A* as a potent epigenetic stimulator that prevents the decommissioning of gene enhancers during UM oncogenesis. Small interfering RNA (siRNA) was performed, and we observed a significant reduction in cell proliferation in UM cell lines when *TFAP2A* was targeted by siRNAs (Fig. 4A), further suggesting that *TFAP2A* is an MTF in UM. To gain insight into the oncogenic properties of *TFAP2A*, we designed two sgRNAs in exon 1 of *TFAP2A* to silence its expression. sgRNAs targeting *TFAP2A* consistently reduced its expression in the OMM2.3 and 92.1 cell lines (Fig. 4B, S10). Similar results were obtained for the tumour-suppressive effect of *TFAP2A* knockdown (KD) using in vitro proliferation and apoptosis assays (Fig. 4C, Fig. S4A, B, Fig. S5). Compared with the control, stable *TFAP2A*-KD in UM cells using CRISPR-Cas9 dramatically compromised the proliferation and promoted the apoptosis of UM cells (Figs. 4C, S4A, B), suggesting the reduced proliferative potential of UM, and we found that it regulated UM cell cycle distribution in vitro (Fig. S4C). We also knocked down *TFAP2A* in 786-O renal cell

carcinoma cells using the same sgRNAs and did not observe its ability to inhibit cell proliferation (Fig. S5). Furthermore, we interfered with *SOX10* expression with siRNA and found no significant change in *TFAP2A* expression (Fig. S6), confirming that *TFAP2A* directly promotes UM formation in vitro. We next evaluated the effect of *TFAP2A* knockdown in vivo in UM cells stably expressing scramble or *TFAP2A*-sgRNAs. *TFAP2A*-KD resulted in a significant decrease in UM tumour growth in vivo (Fig. 4D, E). Taken together, our data strongly suggest that *TFAP2A* is a UM-specific MTF for UM formation and a potential driver of UM progression.

TFAP2A-biologically associated SEs recapitulate the transcriptional machinery of primary tumours

To examine pathways downstream of *TFAP2A*, we used CRISPR-Cas9 to knock out *TFAP2A* expression and conducted RNA-seq experiments. After *TFAP2A* silencing, the expression of 222 genes was significantly elevated, and 212 genes were suppressed (Fig. 5A, B). Notably, SE-mediated transcription was preferentially

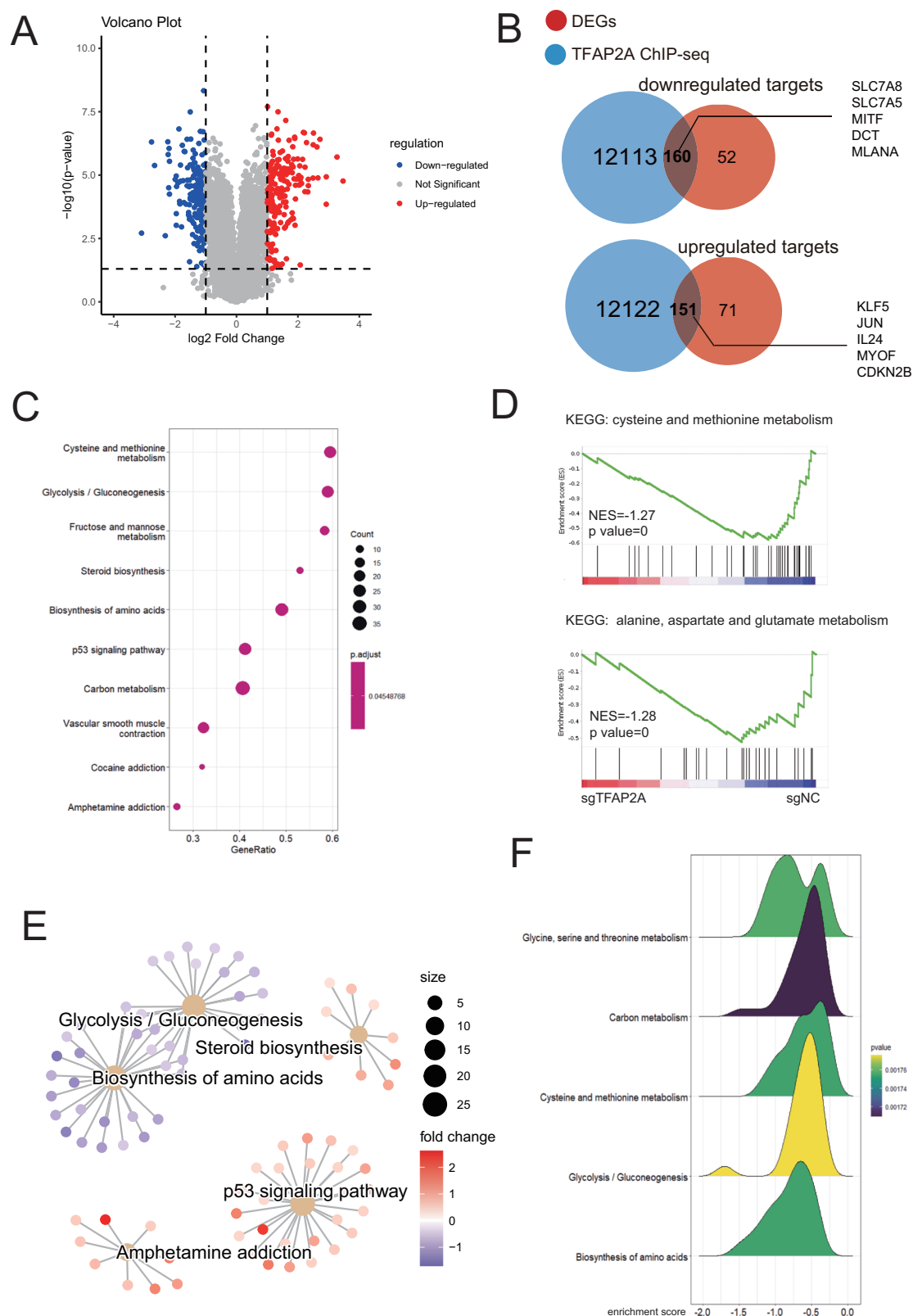


Fig. 5 | Transcriptional analysis revealed key metabolic changes after *TFAP2A* depletion. **A** Volcano plot of gene expression in OMM2.3 sgNC and *TFAP2A*-KD cells. **B** Venn diagram of DEGs (downregulated and upregulated genes) and ChIP-seq *TFAP2A* targets. **C** Pathway analysis of cells stably transfected with the indicated

sgRNA against *TFAP2A*. **D** KEGG analysis of *TFAP2A* expression in cells stably transfected with sgNC and *TFAP2A* sgRNAs. **E** Network combining the GSEA results in the sgNC and sg*TFAP2A* cells. **F** Representative ridge plot of significant pathways in the sgNC and sg*TFAP2A* cells.

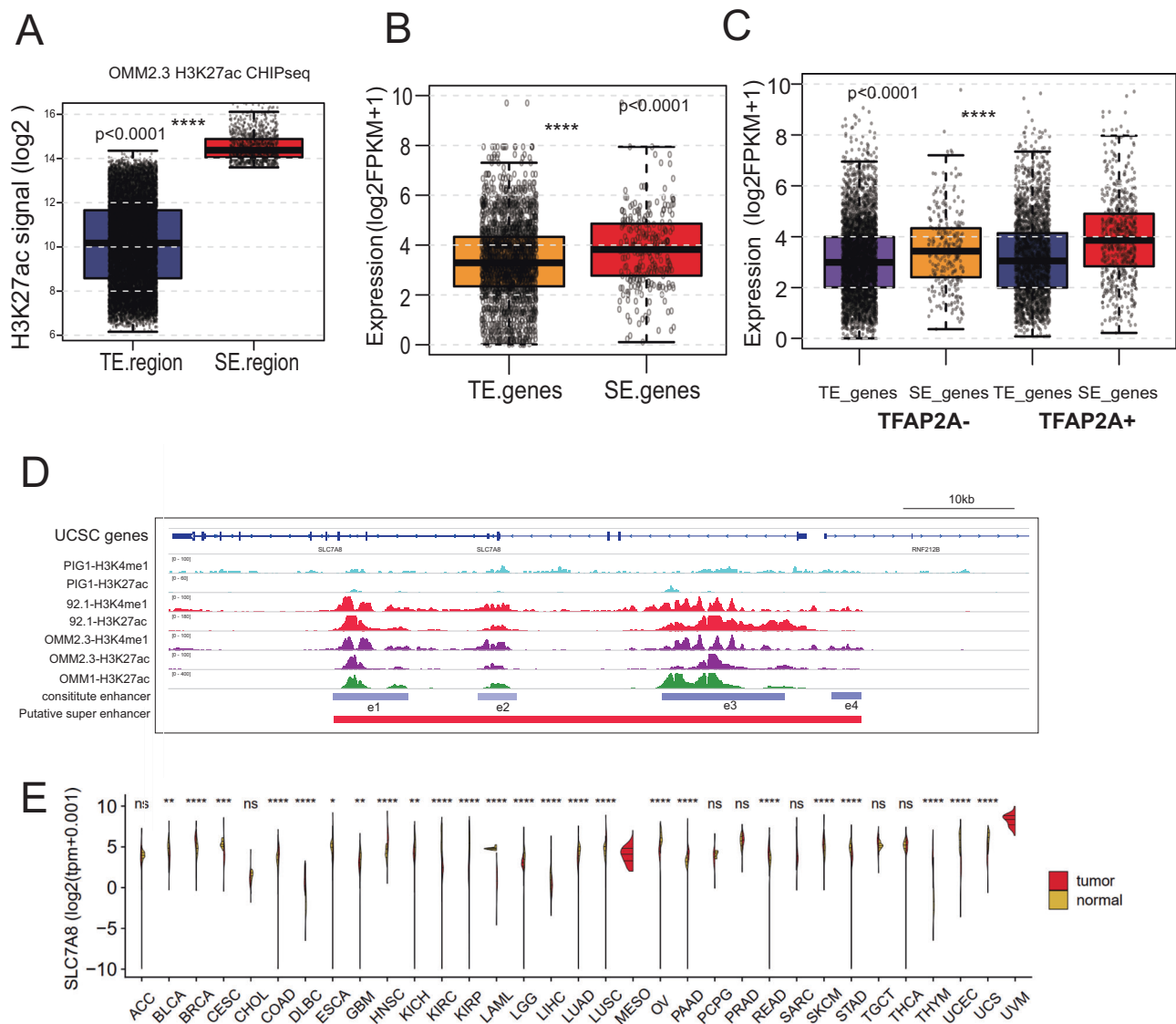


Fig. 6 | TFAP2A orchestrates super enhancer activity. **A** H3K27ac signal in the super enhancer (SE) and typical enhancer (TE) regions in OMM2.3 cells, as revealed by ROSE analysis. **B** Boxplots of SE- and TE-associated gene expression in OMM2.3 cells. **C** TFAP2A-associated gene expression in the TE and SE regions in OMM2.3 cells. RNA expression was normalized using FPKM. **D** IGV plot showing that

SLC7A8-SE regions were enriched in the H3K27ac/H3K4me1 signal and in TFAP2A and EP300 binding sites. **E** Pancancer analysis showing that the expression of SLC7A8 was the highest in the UM dataset. * $P < 0.05$, ** $P < 0.01$, *** $P < 0.001$, **** $P < 0.0001$.

impacted by *TFAP2A* depletion. *TFAP2A* silencing affected the majority of SE gene transcription (Fig. S2D). We next examined the gene expression datasets for verification. The increased expression of these SE target genes in UM was validated via pathway analysis. The functional annotation of *TFAP2A* targets revealed few *TFAP2A*-specific processes, while most were common and strongly associated with translation and metabolism (Fig. 5C). Notably, metabolic processes were highly involved, in which a large category of genes were involved in KEGG HSA00270 CYSTEINE AND METHIONINE METABOLISM and KEGG HSA00250 ALANINE ASPARTATE AND GLUTAMATE METABOLISM (Fig. 5D). The *TFAP2A*-regulated genes were subjected to pathway analysis, which allowed the identification of *TFAP2A* signatures. The *TFAP2A*-associated genes were enriched mostly in metabolic processes such as “biosynthesis of amino acids”, “cysteine and methionine metabolism”, and “metabolic pathways” (Fig. 5E, F). Therefore, we speculated that *TFAP2A* may be involved in the metabolic processes of UM oncogenesis.

Direct activation of SE-associated gene transcription by *TFAP2A*

To gain insight into the relationship between *TFAP2A* enhancer activity and target gene expression, ChIP-seq data were integrated with RNA-seq data to compare SE-associated expression under various conditions. We first compared the enrichment of TE and SE H3K27ac signals in UM cell lines. As defined by ROSE algorithms, SEs are associated with significantly high H3K27ac signals compared with TE regions (Fig. 6A). Notably, the expression of SE-associated genes was significantly greater than that of TE-associated genes (Fig. 6B). In addition, we separated the SE and TE genes on the basis of *TFAP2A* occupancy. Interestingly, we found that *TFAP2A*-associated genes presented much greater gene expression than did genes without *TFAP2A* occupancy, especially SE genes (Fig. 6C), suggesting that *TFAP2A* may promote lineage-specific gene expression through SEs. To explore high-confidence targets of *TFAP2A*, we integrated ChIP-seq and RNA-seq data to identify target genes. We first analysed *TFAP2A* ChIP-seq data and overlapped with SE regions to identify *TFAP2A*-bound SEs in UM cell lines. RNA-seq of genes whose expression was downregulated by *TFAP2A*-KD was subsequently used to identify direct targets of *TFAP2A*.

We distinguished the high and low groups by the median value of the *SLC7A8* expression level. Notably, high *SLC7A8* expression was associated with poor prognosis in the TCGA cohort for overall survival and in the Laurent cohort (GSE22138)²⁹ for metastasis-free survival (Fig. S8), suggesting a potential role for *SLC7A8* in patient survival.

TFAP2A silencing inhibits UM metabolism

We next determined whether *TFAP2A* mediated glucose metabolism under various conditions. As expected, *TFAP2A* silencing dramatically inhibited glycolysis, as determined by lactate secretion analysis. Moreover, *TFAP2A* depletion significantly reduced glutamine and glucose uptake (Fig. 7A, B), indicating that *TFAP2A* silencing inhibited basal energy substance uptake by tumour cells. In addition, GC-MS was used to collect intracellular metabolites from *TFAP2A* wild-type and KD cells ($n = 4$ biological replicates) (Fig. 7C, D). The heatmap showed that *TFAP2A* induced metabolic reprogramming in UM. *SLC7A8* is the prominent downstream node of *TFAP2A* and *SLC7A8* serves as an amino acid transporter in metabolic processes. We determined that the knockdown of *SLC7A8* could impair colony formation and basic metabolite uptake in UM cells, similar to the effects of *TFAP2A*-KD induction (Fig. S9). Our observations support the mechanism that elevated *TFAP2A* expression drives amino acid uptake through *SLC7A8*-mediated pathways (Fig. 7E).

Discussion

Oncogene mutations and chromosomal aberrations are the most recurrent genetic aberrations in primary uveal melanomas³⁰. However, epigenetic aberrations associated with distinct oncogenes and tumour suppressor genes have yet to be elucidated. We conducted an integrative analysis of UM-specific SEs and gene activation patterns to clarify the significance of the regulation of SEs in the characteristics of malignancy. We sought UM-specific SEs to determine whether SEs are responsible for gene regulation in dysfunctional signalling pathways in UM. In particular, we were able to identify UM-specific SE target gene pairings, which are strongly linked to characteristics of malignancy, such as *RASGRP3* and *MITF*^{31–33}. Through a comprehensive analysis of multiomics data, our epigenomic results revealed a highly overexpressed MTF, *TFAP2A*, which has biological significance in accelerating UM tumorigenesis. RNA-sequencing data comparing primary UMs with adjacent normal tissues revealed candidate TFs with robust expression. Our findings suggest that the UM epigenome is characterized by epigenetic aberrations at enhancers that activate a common, aberrant transcriptional program critical for UM growth and survival. Notably, UMs maintain pluripotency while having exceptionally high levels of TFs.

SEs are a specialized clusters of active enhancers densely enriched with regulatory circuitry and active histone marks³⁴. And SEs encompass the strongest potent enhancers connected to the central regulating MTF machinery³⁵. Intriguingly, we found that the core MTF “*TFAP2A*” most frequently occupied the strong enhancer chromatin state. Our findings highlight a melanotic transcriptional program mediated by *TFAP2A* in UM oncogenesis. SE-associated genes were much more highly expressed than typical and normal genes were, and the enhancers hijacked by MTFs were the most highly expressed.

Small-molecule inhibitors or dietary management for targeting cancer metabolism are attractive strategies for anticancer treatment³⁶. In addition to growth hormones, the homeostasis of amino acids (AAs) is critical for the regulation of mTORC1 activity³⁷. In particular, leucine¹⁸ is essential for mTORC1 activation. In a sodium-independent manner, LAT2 is responsible for the intracellular absorption of LNEAA in exchange for glutamine. In addition to identifying the molecular pathways related to UM, our research enabled us to identify a pool of candidates whose expression was strongly associated with UM. Among these proteins, we focused on *SLC7A8*, a putative transcription coregulator whose overexpression in UM has not been previously reported. *SLC7A8* is a key amino acid supplier to the metabolic programs that sustain tumour amino acid metabolism³⁸. In particular, *SLC7A8* is controlled by the master regulator *TFAP2A* and promotes UM oncogenesis by activating metabolic pathways. For the

treatment of advanced UM, overcoming mTORC1 pathway activation might be a potential therapy. Furthermore, the branched-chain amino acid (BCAA) catabolism replenishes the tricarboxylic acid cycle and is dysregulated in UM, whereas targeting essential amino acid (EAA) metabolism might be a novel treatment approach for UM³⁹. In this study, we characterized the epigenomes and metabolome specifically to investigate UM oncogenesis. Detailed characterization of these models might reveal pathways and molecular markers shared by UM.

Moreover, in vitro *TFAP2A* expression in several UM cell lines was reciprocally altered following the modulation of TF function. Consistent with the protumorigenic activity of *TFAP2A* in UM, CRISPR-mediated KD of *TFAP2A* in UM cells decreased cell migration and further inhibited UM tumour growth. The function of *TFAP2A* in cancer remains contentious. In contrast to our findings, early investigations of several malignancies revealed a correlation between high *TFAP2A* expression and melanocyte differentiation²⁸. Besides, *TFAP2A* inhibition led to decreased cell motility and invasion, confirming the involvement of *TFAP2A* as an oncogene. Conversely, the protumorigenic features of *TFAP2A* have been identified in melanomas. We identified *SLC7A8* as a target of *TFAP2A* in UM by integrating transcriptomics and proteomics approaches. *SLC7A8* regulates the cellular transport of BCAAs in exchange for glutamine. High *SLC7A8* expression correlated with UM progression. In addition, the inhibition of LAT-dependent AA transport has yielded encouraging outcomes in pre-clinical models. CRISPR-mediated *TFAP2A* KD reduced *SLC7A8* levels in UM cells, mechanistically linking *TFAP2A* to *SLC7A8* expression through transcriptional regulation. These findings are important for the exploration of cancer therapeutic targets at SEs in UM. By mapping the enhancer landscape and the target in UM, we have uncovered the therapeutic potential of drugs targeting SE-driven transcription and amino acid metabolism in UM.

Data availability

The raw data of RNA-seq, ChIPseq was deposited in Sequence Read Archive in NCBI, <https://www.ncbi.nlm.nih.gov/sra> (PRJNA781290; PRJNA1002592). The datasets analyzed in this study are publicly available: GSE22138 is accessible through NCBI GEO. TCGA data were retrieved via cBioPortal (<https://www.cbioportal.org/>). The raw GC-MS metabolomics data generated in this study, including the results of *TFAP2A*-knockdown and wild-type groups (4 biological replicates each) with 3 quality control (QC) replicates, have been deposited in Figshare repository (<https://doi.org/10.6084/m9.figshare.29036813>). Uncropped western blots are available in Supplementary Fig. S10 of the Supplementary Data file.

Received: 7 December 2023; Accepted: 4 June 2025;

Published online: 23 June 2025

References

1. Jager, M. J. et al. Uveal melanoma. *Nat. Rev. Dis. Prim.* **6**, 24 (2020).
2. Carvajal, R. D. et al. Advances in the clinical management of uveal melanoma. *Nat. Rev. Clin. Oncol.* **20**, 99–115 (2023).
3. Onken, M. D. et al. Oncogenic mutations in GNAQ occur early in uveal melanoma. *Invest. Ophthalmol. Vis. Sci.* **49**, 5230–5234 (2008).
4. Ma, J. et al. Functional characterization of uveal melanoma oncogenes. *Oncogene*. **40**, 806–820 (2021).
5. Johansson, P. A. et al. Whole genome landscapes of uveal melanoma show an ultraviolet radiation signature in iris tumours. *Nat. Commun.* **11**, 2408 (2020).
6. Shain, A. H. et al. The genetic evolution of metastatic uveal melanoma. *Nat. Genet.* **51**, 1123–1130 (2019).
7. Harbour, J. W. et al. Frequent mutation of BAP1 in metastasizing uveal melanomas. *Science*. **330**, 1410–1413 (2010).
8. Onken, M. D. et al. Gene expression profiling in uveal melanoma reveals two molecular classes and predicts metastatic death. *Cancer Res.* **64**, 7205–7209 (2004).

9. Gu, X. et al. Epigenetic drug library screening reveals targeting DOT1L abrogates NAD(+) synthesis by reprogramming H3K79 methylation in uveal melanoma. *J. Pharm. Anal.* **13**, 24–38 (2023).
10. Chai, P. et al. Regulation of epigenetic homeostasis in uveal melanoma and retinoblastoma. *Prog. Retin. Eye. Res.* **89**, 101030 (2022).
11. Hou, P. et al. Machine learning-based integrative analysis of methylome and transcriptome identifies novel prognostic DNA methylation signature in uveal melanoma. *Brief. Bioinform.* **22**, bbaa371 (2021).
12. Bakhoum, M. F. et al. Loss of polycomb repressive complex 1 activity and chromosomal instability drive uveal melanoma progression. *Nat. Commun.* **12**, 5402 (2021).
13. Landreville, S. et al. Histone deacetylase inhibitors induce growth arrest and differentiation in uveal melanoma. *Clin. Cancer. Res.* **18**, 408–416 (2012).
14. Zhang, G. M. et al. Reciprocal positive regulation between BRD4 and YAP in GNAQ-mutant uveal melanoma cells confers sensitivity to BET inhibitors. *Pharm. Res.* **184**, 106464 (2022).
15. Xie, F. et al. Targeting FOXM1 condensates reduces breast tumour growth and metastasis. *Nature*. **638**, 1112–1121 (2025).
16. Liu, S. et al. Effects of super-enhancers in cancer metastasis: mechanisms and therapeutic targets. *Mol. Cancer*. **23**, 122 (2024).
17. Huang, H. et al. Defining super-enhancer landscape in triple-negative breast cancer by multiomic profiling. *Nat. Commun.* **12**, 2242 (2021).
18. Liang, H. C. et al. Super-enhancer-based identification of a BATF3/IL-2R-module reveals vulnerabilities in anaplastic large cell lymphoma. *Nat. Commun.* **12**, 5577 (2021).
19. Sim, N. et al. TWEAK/Fn14 signalling driven super-enhancer reprogramming promotes pro-metastatic metabolic rewiring in triple-negative breast cancer. *Nat. Commun.* **15**, 5638 (2024).
20. Ye, B. et al. Oncogenic enhancers drive esophageal squamous cell carcinogenesis and metastasis. *Nat. Commun.* **12**, 4457 (2021).
21. Li, Q. L. et al. Genome-wide profiling in colorectal cancer identifies PHF19 and TBC1D16 as oncogenic super enhancers. *Nat. Commun.* **12**, 6407 (2021).
22. Sui, Y. et al. Targeting super-enhancer-driven transcriptional dependencies suppresses aberrant Hedgehog pathway activation and overcomes smoothened inhibitor resistance. *Cancer. Res.* **84**, 2690–2706 (2024).
23. Gryder, B. E. et al. PAX3-FOXO1 establishes myogenic super enhancers and confers BET bromodomain vulnerability. *Cancer. Discov.* **7**, 884–899 (2017).
24. Martin, M. Cutadapt removes adapter sequences from high-throughput sequencing reads. *EMBnet. J.* **17**, 10–12 (2011).
25. Li, S. et al. Facilitating integrative and personalized oncology omics analysis with UCSCXenaShiny. *Commun. Biol.* **7**, 1200 (2024).
26. Kaya-Okur, H. S. et al. CUT&Tag for efficient epigenomic profiling of small samples and single cells. *Nat. Commun.* **10**, 1930 (2019).
27. Xiong, L. et al. Aberrant enhancer hypomethylation contributes to hepatic carcinogenesis through global transcriptional reprogramming. *Nat. Commun.* **10**, 335 (2019).
28. Seberg, H. E. et al. TFAP2 paralogs regulate melanocyte differentiation in parallel with MITF. *PLoS. Genet.* **13**, e1006636 (2017).
29. Laurent, C. et al. High PTP4A3 phosphatase expression correlates with metastatic risk in uveal melanoma patients. *Cancer. Res.* **71**, 666–674 (2011).
30. Robertson, A. G. et al. Integrative analysis identifies four molecular and clinical subsets in uveal melanoma. *Cancer. Cell.* **32**, 204–220 e215 (2017).
31. Chen, X. et al. RasGRP3 mediates MAPK pathway activation in GNAQ mutant uveal melanoma. *Cancer. Cell.* **31**, 685–696 e686 (2017).
32. Moore, A. R. et al. GNA11 Q209L mouse model reveals RasGRP3 as an essential signaling node in uveal melanoma. *Cell. Rep.* **33**, 108277 (2020).
33. Phelps, G. B. et al. MITF deficiency accelerates GNAQ-driven uveal melanoma. *Proc. Natl Acad. Sci. USA* **119**, e2107006119 (2022).
34. Bal, E. et al. Super-enhancer hypermutation alters oncogene expression in B cell lymphoma. *Nature*. **607**, 808–815 (2022).
35. Gryder, B. E. et al. Chemical genomics reveals histone deacetylases are required for core regulatory transcription. *Nat. Commun.* **10**, 3004 (2019).
36. Sciacovelli, M. et al. Dynamic partitioning of branched-chain amino acids-derived nitrogen supports renal cancer progression. *Nat. Commun.* **13**, 7830 (2022).
37. Elorza, A. et al. HIF2alpha acts as an mTORC1 activator through the amino acid carrier SLC7A5. *Mol. Cell.* **48**, 681–691 (2012).
38. Bassi, M. T. et al. SLC7A8, a gene mapping within the lysinuric protein intolerance critical region, encodes a new member of the glycoprotein-associated amino acid transporter family. *Genomics*. **62**, 297–303 (1999).
39. Yue, M. et al. Oncogenic MYC activates a feedforward regulatory loop promoting essential amino acid metabolism and tumorigenesis. *Cell. Rep.* **21**, 3819–3832 (2017).

Acknowledgements

This study was supported by the Science and Technology Commission of Shanghai (20DZ2270800, 23ZR1438400), National Key Clinical Specialty of China, Shanghai Eye Disease Research Center (2022ZZ01003).

Author contributions

A.Z., Y.W., and X.X. designed the experiments. H.P., W.S. and H.W. performed the experiments and interpreted the results. S.G. and L.Z. assisted with the data analysis. H.P. and W.S. wrote the manuscript. A.Z. reviewed and revised the manuscript.

Competing interests

The authors declare no competing interests.

Ethical approval and consent to participate

This study was approved by the ethics committee of Shanghai Ninth People's hospital.

Additional information

Supplementary information The online version contains supplementary material available at <https://doi.org/10.1038/s42003-025-08338-8>.

Correspondence and requests for materials should be addressed to Xiaofang Xu, Yefei Wang or Ai Zhuang.

Peer review information *Communications Biology* thanks the anonymous reviewers for their contribution to the peer review of this work. Primary Handling Editors: Silvia Belluti and Johannes Stortz.

Reprints and permissions information is available at <http://www.nature.com/reprints>

Publisher's note Springer Nature remains neutral with regard to jurisdictional claims in published maps and institutional affiliations.

Open Access This article is licensed under a Creative Commons Attribution-NonCommercial-NoDerivatives 4.0 International License, which permits any non-commercial use, sharing, distribution and reproduction in any medium or format, as long as you give appropriate credit to the original author(s) and the source, provide a link to the Creative Commons licence, and indicate if you modified the licensed material. You do not have permission under this licence to share adapted material derived from this article or parts of it. The images or other third party material in this article are included in the article's Creative Commons licence, unless indicated otherwise in a credit line to the material. If material is not included in the article's Creative Commons licence and your intended use is not permitted by statutory regulation or exceeds the permitted use, you will need to obtain permission directly from the copyright holder. To view a copy of this licence, visit <http://creativecommons.org/licenses/by-nc-nd/4.0/>.

© The Author(s) 2025